Characterization of the Si:Se$^+$ Spin-Photon Interface

Adam DeAbreu,[1] Camille Bowness,[1] Rohan J.S. Abraham,[1] Alzbeta Medvedova,[1] Kevin J. Morse,[1]
Helge Riemann,[2] Nikolay V. Abrosimov,[2] Peter Becker,[3] Hans-Joachim Pohl,[4] Michael L.W. Thewalt,[1]
and Stephanie Simmons[1,*]

[1]*Department of Physics, Simon Fraser University, 8888 University Drive, Burnaby,
British Columbia V5A 1S6, Canada*
[2]*Leibniz-Institut für Kristallzüchtung, Max-Born-Straße 2, 12489 Berlin, Germany*
[3]*Physikalisch-Technische Bundesanstalt (PTB) Braunschweig, Bundesallee 100, 38116 Braunschweig, Germany*
[4]*VITCON Projectconsult GmbH, Otto-Schott Straße 13, 07745 Jena, Germany*

Silicon is the most-developed electronic and photonic technological platform and hosts some of the highest-performance spin and photonic qubits developed to date. A hybrid quantum technology harnessing an efficient spin-photon interface in silicon would unlock considerable potential by enabling ultralong-lived photonic memories, distributed quantum networks, microwave-to-optical photon converters, and spin-based quantum processors, all linked with integrated silicon photonics. However, the indirect band gap of silicon makes identification of efficient spin-photon interfaces nontrivial. Here we build upon the recent identification of chalcogen donors as a promising spin-photon interface in silicon. We determine that the spin-dependent optical degree of freedom has a transition dipole moment stronger than previously thought [here 1.96(8) D], and the spin T_1 lifetime in low magnetic fields is longer than previously thought [here longer than 4.6(1.5) h]. We furthermore determine the optical excited-state lifetime [7.7(4) ns], and therefore the natural radiative efficiency [0.80(9)%], and by measuring the phonon sideband determine the zero-phonon emission fraction [16(1)%]. Taken together, these parameters indicate that an integrated quantum optoelectronic platform based on chalcogen-donor qubits in silicon is well within reach of current capabilities.

I. INTRODUCTION

A future quantum technology, wherein stored quantum information is communicated over a quantum network, will necessarily involve both matter-based qubits and optical photons. In pursuit of this aim, many potential spin-photon interfaces are being actively developed [1–3]. A wide array of defects in semiconductors and insulators have attracted attention because of their favorable optical and spin characteristics. These include quantum dots in III-V heterostructures [4], nitrogen-vacancy [5] and silicon-vacancy [6] centers in diamond, rare-earth ions in insulators such as Nd-doped yttrium orthosilicate [7] and Er-doped yttrium orthosilicate [8], defects in SiC [9,10], single impurities in ZnSe [11–13], and donors in ZnO [14]. Notable in its absence from this list is silicon, which, when

isotopically purified to ^{28}Si, is host to some of the longest-lived and highest-fidelity spin qubits studied to date [15–18]. Silicon offers high-performance integrated single-photon detectors [19] in addition to an expansive selection of high-quality photonic components [20,21] due to decades of fabrication-process development. Furthermore, silicon has a strong $\chi^{(3)}$ nonlinearity and large refractive index that enables dense packing of photonic circuitry. Despite the considerable advantages of these two quantum silicon platforms, unifying these technologies through an efficient spin-photon interface has proven elusive.

A few paramagnetic centers in silicon possess spin-dependent optical transitions, including shallow donor-bound excitons [22] and orbital transitions in rare-earth ions, such as erbium [23]. However, in the aforementioned cases, the defects couple only weakly to light as determined by their small optical transition dipole moments. Although recent work has demonstrated evanescent coupling of defects with strong transition dipole moments in materials placed adjacent to silicon photonic structures [24], the coupling strengths and photon-collection efficiencies are inherently limited in such designs.

---

*s.simmons@sfu.ca

The ideal silicon spin-photon interface would be a natively integrated optical center that possesses a long-lived spin, a large transition dipole moment, and a high radiative efficiency. In this work we demonstrate that singly ionized deep chalcogen donors in silicon possess a strong light-matter interaction, which is suitable for strong coupling to silicon photonic cavities at the single-spin level. This offers a clear path toward chalcogen-based integrated silicon quantum optoelectronics.

The optical characteristics of substitutional chalcogen donors (specifically sulfur, selenium, and tellurium) have been studied for decades [25–29]. It was identified that the natural distribution of silicon and chalcogen isotopes act as sources of static inhomogeneity in the bulk. Consequently, ultrasharp optical linewidths, on the order of microelectronvolts can be achieved [29] by working with ensembles of individual chalcogen isotopes in isotopically purified ^{28}Si. This remarkable uniformity allowed the hyperfine splitting and the electron spin g value of the $1s{:}A$ ground state of singly ionized ^{77}Se to be directly observed through optical excitation into the first excited state, $1s{:}T_2{:}\Gamma_7$. Following this, initial electron-spin characterization at X-band microwave frequencies of ^{77}Se$^+$ demonstrated promising electron-spin qubit coherence and lifetime characteristics [30] similar to those of the shallow donors' ultralong-lived electron spins.

The identification of singly ionized chalcogen donors as a promising spin-photon interface in silicon was made only relatively recently [31], and bounds on some key spin and optical parameters of ^{77}Se$^+$ were determined to support this proposal. Key parameters in Ref. [31] included lower bounds on the spin T_1 lifetime [greater than 6.2(4) min], the optical transition dipole moment [greater than 0.77 D], and the optical excited-state lifetime [greater than 5.5 ns], as well as an upper bound on the calculated radiative lifetime [less than 39 μs]. In this work we improve on the bound of the spin T_1 lifetime [greater than 4.6(1.5) h] and determine the transition dipole moment [1.96(8) D]. Furthermore, we offer insights into the optical transition of interest by reporting the phonon sideband profile and zero-phonon-line (ZPL) fraction [16(1)%] and a direct measurement of the excited-state lifetime [7.7(4) ns], and hence the total radiative efficiency [0.80(9)%]. Lastly, we precisely determine the location of the second excited state in the neutral charge state of Se by performing Raman spectroscopy. The experimental results presented in Sec. II are structured in that order.

A. The ^{28}Si:^{77}Se$^+$ spin-photon system

Substitutional selenium atoms in silicon are deep double donors. When singly ionized, the unpaired spin-$\frac{1}{2}$ electron possesses a hydrogenic orbital structure with a $1s$ ground state. The sixfold degeneracy of the conduction band and the two electron spin states give rise to 12 $1s$ levels, which are split by a combination of central-cell, valley-orbit, and spin-orbit effects. The spin and photon degrees of freedom relevant to this work are all contained within these 12 electronic $1s$ levels.

The ground state, $1s{:}A$, possesses two degenerate electron spin levels and has a binding energy of approximately 593 meV [27]. The first orbital excited states, labeled $1s{:}T_2$, are split into components labeled $1s{:}T_2{:}\Gamma_7$ and $1s{:}T_2{:}\Gamma_8$, the lower of which, $1s{:}T_2{:}\Gamma_7$, possesses two spin-orbit levels and has a binding energy of approximately 166 meV [27]. The remaining $1s$ levels, labeled $1s{:}E$, are thought to lie above $1s{:}T_2{:}\Gamma_8$, as is the case for the neutral charge state Se^0 and the group-V shallow donors, but have not been observed in Se$^+$ [see Fig. 1(a)]. The optical transitions between $1s{:}A$ and $1s{:}T_2{:}\Gamma_7$ are forbidden according to effective-mass theory (EMT) but are symmetry allowed, and are at approximately 427 meV, or 2.9 μm [27], which is in the midinfrared optical band. Further details on the orbital structure of this system are given in Ref. [31].

Additionally, the ^{77}Se$^+$ isotope possesses a spin-$\frac{1}{2}$ nuclear spin and a corresponding $A \approx 1.66$ GHz hyperfine interaction [29,31] within the $1s{:}A$ electronic manifold. This gives rise to a ground-state spin Hamiltonian shared with that of the neutral shallow donor ^{31}P and given by

$$\mathcal{H} = \frac{g_e\mu_B}{h}B_0 S_z - \frac{g_n\mu_N}{h}B_0 I_z + A\vec{S}\cdot\vec{I}, \qquad (1)$$

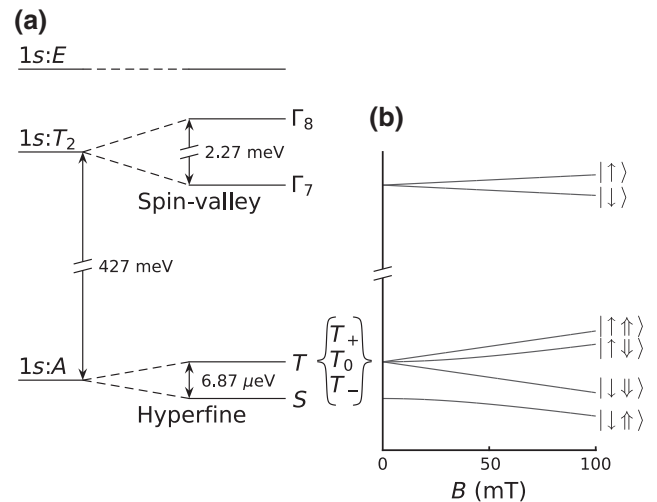where A, the hyperfine constant, and g_e (2.0057) and g_n (1.07), the electron and nuclear g factors, respectively, are

FIG. 1. Energy-level diagram of the Si:^{77}Se$^+$ system. (a) The six $1s{:}T_2$ levels are split into $1s{:}T_2{:}\Gamma_7$ (two states) and $1s{:}T_2{:}\Gamma_8$ (four states) by the spin-valley interaction. With nuclear spin interactions, the $1s{:}A$ states are split by the hyperfine interaction into electron-nuclear spin singlet, S, and triplet, T (T_-, T_0, T_+), states. (b) These eigenstates change according to an applied magnetic field. In the high-field limit, the $1s{:}A$ and $1s{:}\Gamma_7$ states are labeled according to nuclear spin ($\Uparrow$, $\Downarrow$) and electron spin ($\uparrow$, $\downarrow$).

specific to $^{77}Se^+$. Here μ_B and μ_N are the Bohr and nuclear magnetons, h is the Planck constant, and $\vec{S}$ and $\vec{I}$ are the spin operators of the electron and the nucleus. At zero magnetic field, this spin Hamiltonian results in a splitting of 1s:A energy levels defined by electron-nuclear spin singlet and triplet states [see Fig. 1(b)]. The 1s:T_2:Γ_7 state possesses no such splitting and therefore these levels form a lambda transition [27] which can be spectrally resolved in the bulk [29,31]. The allowed magnetic resonance transitions from the singlet state S_0 to the triplet states T_-, T_0, T_+ support long-lived qubits [31], particularly across the $S_0 \Leftrightarrow T_0$ transition, which is a "clock transition" [32] at zero field.

II. EXPERIMENTAL RESULTS

A. Singlet-triplet T_1 temperature dependence

The spin equilibration time constant, T_1, of the $^{77}Se^+$ singlet-triplet qubit in Earth's magnetic field and at low temperatures (1.6 K) was previously found to be approximately 6 min [31]. Although already quite long, this T_1 time is shorter than the approximately-30-min electron T_1 of ^{31}P measured at 1.6 K and 0.35 T, as well as significantly shorter than the projected electron T_1 times available to ^{31}P at 1.6 K in Earth's magnetic field [33]. Six minutes is substantially longer than previously measured $^{77}Se^+$ electron T_1 times collected at higher temperatures [30], but shorter than the projected T_1 lifetime (approximately 337 h) following a T^9 dependence fitted from these higher-temperature data and extrapolated to 1.6 K (see Fig. 2). Here we elucidate the decay mechanisms affecting the $^{77}Se^+$ singlet-triplet qubit and determine an experimental regime that gives rise to a 276(90)-min [4.6(1.5)-h] T_1 lifetime.

The similarities between the ^{31}P system and the $^{77}Se^+$ system imply that a number of known ^{31}P electron T_1 decay mechanisms, such as the direct [33], Raman [34], and concentration-dependent decay mechanisms with concentrations above 10^{16} cm^{-3} [33], can apply to $^{77}Se^+$. The much larger valley-orbit splitting between the ground 1s:A state and first excited state 1s:T_2:Γ_7 of $^{77}Se^+$ — at least 7 times greater than the maximum phonon energy — implies that the Orbach decay mechanism [35] known to apply to ^{31}P is irrelevant in the case of $^{77}Se^+$.

An additional decay mechanism is known to contribute to the T_1 decay of $^{77}Se^+$ [31]: incident room-temperature blackbody radiation possesses sufficient energy to ionize both neutral and singly ionized ^{77}Se, directly affecting T_1 via time-varying local charge configurations. Under our experimental conditions, blackbody radiation generated within the cryogenic apparatus is negligible compared with the room-temperature incident blackbody radiation optically coupled to the sample. Correspondingly, this blackbody T_1 decay mechanism is largely independent of the sample temperature. In contrast, the direct and
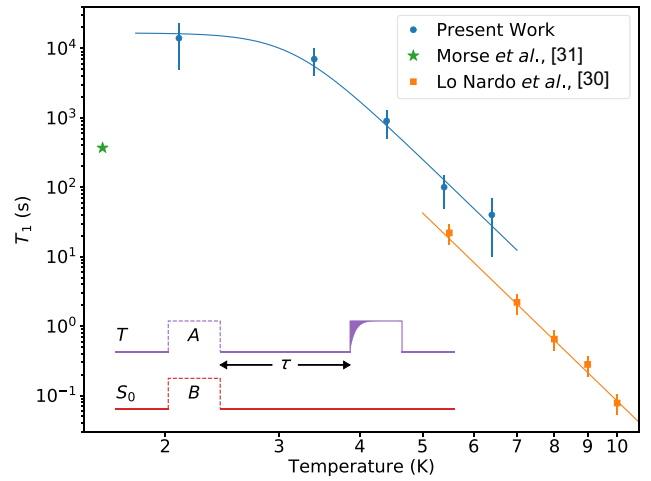

FIG. 2. Temperature dependence of $^{77}Se^+$ electron-nuclear spin singlet-triplet T_1 taken near Earth's magnetic field (blue), revealing a low-temperature limit of $T_1 = 4.6(1.5)$ h, and comparison with published data, collected with less blackbody shielding (green asterisk) (reprinted from Ref. [31] with permission), as well as electron spin T_1 data taken at 0.35 T (orange line) (reprinted from Ref. [30] with permission). The inset shows the optical pumping and read-out sequence to measure singlet-triplet T_1. For a given wait time, τ, the total remaining polarization signal is measured as the difference between two integrated absorption transient areas, both measuring the population of the triplet state (solid line), after two different initialization pulses (dashed lines). First (A) after initialization into the singlet by pumping on the 1s:A:$T \Leftrightarrow$ 1s:T_2:Γ_7 transition, here labeled T, and second (B) after initialization into the triplet by pumping on the 1s:A:$S_0 \Leftrightarrow$ 1s:T_2:Γ_7 transition, here labeled S_0.

Raman decay mechanisms display a $1/T$ and $1/T^9$ temperature dependence, respectively [33,34]. Measurements of the electron T_1 in a low-concentration (approximately 2×10^{13} cm^{-3}) $^{77}Se^+$ bulk sample (sample ^{28}Si:^{77}Se:LB (Low Boron); see Supplemental Material [36]) as a function of temperature are used to determine the prevalence of these possible mechanisms.

The experimental setup follows closely the setup presented in Ref. [31] with additional filters in place to minimize room-temperature blackbody effects: optical band-pass filters centered at 2.9 μm as well as neutral-density filters are mounted within the cryogenic assembly in the optical beam path, and the sample is shielded from room-temperature blackbody radiation from all other directions.

The singlet-triplet qubit is initialized by resonantly pumping one arm of the lambda transition, for example, initializing it into the singlet state by selectively pumping 1s:A:$T \Leftrightarrow$ 1s:T_2:Γ_7, as described in Ref. [31]. Following this, a mechanical shutter blocks the resonant light. After a chosen delay, the remaining spin hyperpolarization is measured by recording the absorption transient of unblocked resonant light (see the inset in Fig. 2). For a given delay

time, two different measurements are taken, and the difference between their absorption transients constitutes the measured signal. The first of these measurements hyperpolarizes into the singlet state and the second hyperpolarizes into the triplet state. Both measurements' absorption transients consistently probe the final triplet population. This subtraction method ensures that the signal necessarily decays to zero in the long-delay limit where the spins reach equilibrium. The singlet-triplet T_1 lifetime at a given temperature is determined by iterating this measurement with different delay times.

The temperature dependence of T_1 over the range from 2.1 to 6.4 K is shown in Fig. 2. The data are well fit by $1/T_1 = AT^9 + B$, with $A = 2.0(3) \times 10^{-9}$ s^{-1} K^{-9} representing a T^9 Raman process in agreement with data taken at 0.35 T [30], which is fit well by $1/T_1 = CT^9$ ($C = 1.2 \times 10^{-8}$ s^{-1} K^{-9}). Additionally, there is a temperature-independent contribution with a low-temperature limit of $T_1 = 4.6(1.5)$ h most likely due to a residual blackbody-related decay process dominating below 2K. The disagreement near 5 K may be due to temperature offsets between these two different experimental setups; alternatively, although the T^9 relaxation process is expected to be independent of the magnetic field for electron spins [34], this may not apply when comparing singlet-triplet spin qubits and nearly pure electron spin qubits. These trends indicate that a spin T_1 of 19 ± 3 min is available at the easily accessible temperature of 4.2 K.

B. Absorption

In this section we present measurements based on optical absorption spectra. We improve on previous transition-dipole-moment estimates, and use these data to provide a concentration conversion factor.

1. Transition dipole moment

The optical interaction strength of a spin-photon interface is characterized by its transition dipole moment, μ. The dipole moment can be calculated from the absorption spectrum of a bulk sample, combined with an accurate defect concentration value, and a known optical path length [36]. Previous work [31] employed a bulk sample with nonuniform ^{77}Se$^+$ concentration and consequently only lower bounds on the transition dipole moment could be made.

Here we calculate the transition dipole moment using a selenium-diffused, ^{28}Si:^{77}Se, wafer sample (sample w^{28}Si:^{77}Se:IB (Intermediate Boron); see Supplemental Material [36]). The absorption spectrum is measured with a Bruker IFS 125HR Fourier-transform infrared (FTIR) spectrometer with gold mirrors, a KBr beam splitter, and a mercury-cadmium-telluride (MCT) detector to obtain an absorption-coefficient spectrum of the Se$^+$ $1s{:}A \Rightarrow$

$1s{:}T_2{:}\Gamma_7$ transition, where the absorption coefficient spectra is calculated according to

$$\alpha = \frac{-1}{L}\ln\left(\frac{I_s}{I_0}\right), \qquad (2)$$

where I_s and I_0 are FTIR spectra with and without the sample in the beam path, respectively, and L is the length of the sample.

This sample is confirmed to have a near-uniform Se$^+$ concentration by observing the complete compensation of all boron in the sample [36]. In this case one might expect the Se$^+$ concentration is equivalent to the B concentration throughout the sample; however, the precise distribution of donors and acceptors in the sample may modify this value. To measure the Se$^+$ concentration precisely, we use a tip-angle measurement [16], whose details were described in Ref. [31]. We measure a Se$^+$ concentration of $5.2(4) \times 10^{14}$ cm^{-3}, which is less than the measured B concentration of $5.9(8) \times 10^{14}$ cm^{-3}, likely indicating the presence of doubly ionized selenium, Se^{2+}, or ionized selenium pairs, Se$_2^{+/2+}$. Combining this with the absorption-coefficient spectrum, we calculate a transition dipole moment, μ, of 1.96(8) D [36]. This value is more than a factor of 2 higher than the previously established lower bound.

2. Selenium conversion factor

From the tip-angle concentration measurement and absorption-coefficient spectrum, we determine a conversion factor,

$$f = \frac{c_{\mathrm{Se}^+}}{\int \alpha \, d\nu} = 6.2(5) \times 10^{14} \text{ cm}^{-1}, \qquad (3)$$

for the $1s{:}A \Rightarrow 1s{:}T_2{:}\Gamma_7$ zero-phonon spectral line, where $\int \alpha \, d\nu$ is the integrated absorption-coefficient spectrum of the zero-phonon spectral line. Peak conversion factors, $k_{\mathrm{Se}^+} = c_{\mathrm{Se}^+}/\alpha_{\max}$, are tabulated in the Supplemental Material [36].

C. Photoluminescence

The radiative properties − both the radiative efficiency and the zero-phonon-line fraction − of the Se$^+$ spin-photon interface have not been previously established. In this section we report the observation of the phonon-assisted luminescence sideband of the $1s{:}T_2{:}\Gamma_7 \Rightarrow 1s{:}A$ optical transition, which reveals a zero-phonon-line fraction of 16(1)%. Subsequently we measure the excited-state lifetime [7.7(4) ns] and compare this with the calculated radiative lifetime to infer a radiative efficiency of 0.80(9)%.

1. Zero-phonon-line fraction

Photoluminescence spectra are obtained with a Bruker IFS 125HR FTIR spectrometer with gold mirrors, a CaF$_2$

beam splitter, and a liquid-nitrogen-cooled InSb detector with a 2440-nm long-pass filter. A high-Se$^+$-concentration sample (w^{nat}Si:^{nat}Se:HB (High Boron); see Supplemental Material [36]) is pumped with 1 W of laser light resonant with the Se$^+$ $1s$:$A \Rightarrow 2p_\pm$ transition (4578 cm^{-1}, or 2184 nm), which is generated with a Cr^{2+}:ZnS/Se narrow-band tunable laser pumped by an erbium fiber laser (IPG Photonics) operating at 1567 nm. From the excited state $2p_\pm$, the electron can decay via phonon cascade to $1s$:T_2:Γ_7 followed by photon emission to $1s$:A.

The resulting photoluminescence spectrum, including the phonon-assisted sideband, is shown in Fig. 3. The integrated phonon sideband is 5.6 times larger than the area of the zero-phonon line, resulting in a ZPL-fraction lower bound of 15%. After correction for reabsorption of light given the known ZPL transition dipole moment, which will disproportionately affect the integrated area of the ZPL, we obtain a ZPL fraction of 16(1)%.

The total radiative lifetime includes both the zero-phonon and the phonon-assisted radiative pathways, resulting in a total calculated radiative lifetime τ of 0.90(7) μs [36].

2. Excited-state lifetime and radiative efficiency

The decay of the $1s$:T_2:Γ_7 valley state to the ground state $1s$:A can occur through purely radiative, phonon-assisted radiative, and fully nonradiative pathways. The ratio of the measured $1s$:T_2:Γ_7 excited-state lifetime to the calculated radiative lifetime reveals the technologically consequential radiative efficiency of this spin-photon interface.
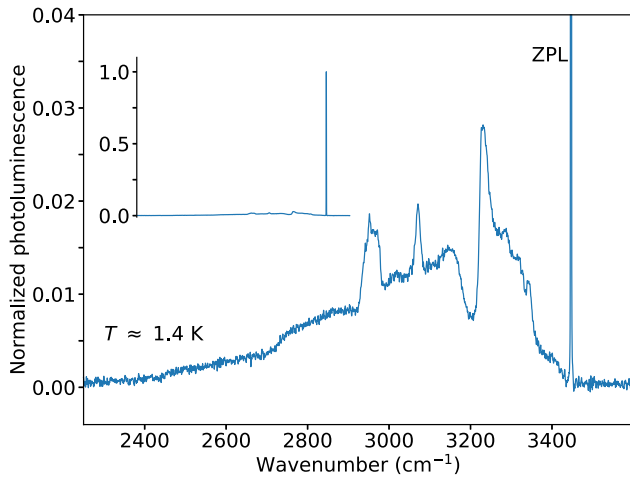
FIG. 3. The photoluminescence spectrum of the Se$^+$ $1s$:T_2:$\Gamma_7 \Rightarrow 1s$:A transition taken with a spectral resolution of 1 cm^{-1}. The inset shows the normalized spectrum showing the relative height of the ZPL to the phonon sideband. The main panel shows the same spectrum, clipped vertically to display the phonon sideband features. The area of the phonon sideband is 5.6 times larger than the area of the ZPL, revealing a reabsorption-corrected ZPL fraction of 16(1)%.
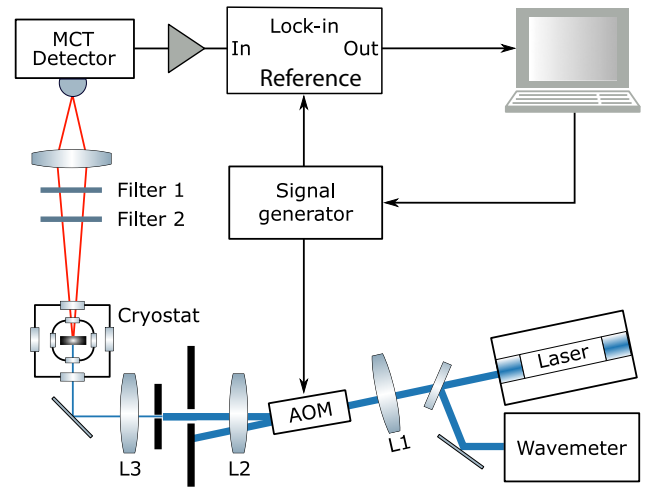
FIG. 4. Experimental setup. A laser, tuned to the Se$^+$ $1s$:$A \Rightarrow 2p_\pm$ transition (4578 cm^{-1}, or 2184 nm), whose wavelength is monitored with a pick-off beam routed into a wavemeter, is focused through a lens (L1) to minimize the beam waist within a 10-MHz-bandwidth germanium AOM. The first diffracted (modulated) beam is recollimated (L2) and passed through a 1-mm aperture, to reject the main beam and higher-order diffracted beams, and focused (L3) onto the w^{nat}Si:^{nat}Se:HB sample held in superfluid helium. A portion of the resulting $1s$:T_2:$\Gamma_7 \Rightarrow 1s$:A luminescence signal is captured by an elliptical mirror and sent through 2440- and 2850-nm long-pass filters (Filter 1 and Filter 2), to selectively pass $1s$:T_2:$\Gamma_7 \Rightarrow 1s$:A light onto a MCT detector. A lock-in measurement was applied to the detected signal with the use of the AOM driving frequency as the reference.

Conventional methods of directly measuring a total luminescence lifetime use optical pulses and time-resolved, high-sensitivity detectors that are at least comparable in speed with the transition lifetime of interest. Such sources and detectors are not yet routinely available in the 2.9-μm region. Hence, before this work, only lower bounds on the total lifetime of this center were known. Hole-burning measurements, limited by FTIR-spectrometer resolution, indicated a total excited-state lifetime longer than 5.5 ns [31], corresponding to a homogeneous linewidth smaller than 0.001 cm^{-1}.

To directly measure the excited-state lifetime, we perform a modulated-excitation experiment [37] using a continuous-wave, single-frequency laser modulated by an acousto-optic modulator (AOM). The measurement configuration is shown in Fig. 4.

The laser is brought into resonance with the $1s$:$A \Rightarrow 2p_\pm$ transition (4578 cm^{-1}, or 2184 nm), as described in Sec. II C 1, for efficient pumping to $1s$:T_2:Γ_7 via the $2p_\pm$ state. This pump laser is sinusoidally modulated with a germanium AOM (IntraAction AGM-802A9) with a nominal bandwidth of 10 MHz, which is increased to 20 MHz by reducing the laser spot size using a converging lens pair. Approximately 400 mW of laser light is incident on the

sample. The resulting $1s$:T_2:$\Gamma_7 \Rightarrow 1s$:A luminescence from the sample w^{nat}Si:^{nat}Se : HB (see Supplemental Material [36]) is spectrally filtered and detected with a MCT detector (VIGO Systems, PVI-4TE-1-0.5x0.5) and fed into a lock-in amplifier with the AOM modulation drive as its reference.

After correction for the instrumental frequency response by measuring scattered pump-laser light, the frequency dependence of the resulting signal reveals the excited-state lifetime. At frequencies much lower than the inverse of the excited-state lifetime, the system has time to equilibrate and a high ac photoluminescence signal is detected, whereas at higher frequencies the ac signal amplitude will drop. Alternatively put, the system behaves as a low-pass filter with a characteristic amplitude (A) and phase (Θ) response, as a function of modulation frequency, f, given by [37]

$$A = \frac{1}{[1 + (2\pi f \ T_1)^2]^{1/2}}, \qquad (4)$$

$$\Theta = -\tan^{-1}(2\pi f \ T_1), \qquad (5)$$

where T_1 is the decay time of the optically excited state. The resulting data, corrected for the system response, are shown in Fig. 5. The characteristic amplitude and phase drop-off points, at $1/\sqrt{2}$ and $45°$, agree and reveal a T_1 lifetime for the $1s$:T_2:Γ_7 excited state of 7.7(4) ns. This is much shorter than the calculated radiative lifetime of 0.90(7) μs, meaning the decay is dominated by nonradiative decay mechanisms. By taking the ratio, we determine a radiative efficiency of 0.80(9)%.

From the T_1 value we determine a homogeneous linewidth of 0.00069(4) cm^{-1}; however, as thermally activated transitions to higher excited states are possible [31], this homogeneous linewidth is likely to be a lower bound. For the purposes of estimating coupling cooperativity [36] between the Se$^+$ $1s$:$A \Leftrightarrow 1s$:T_2 : Γ_7 transition and a photonic cavity, we use the upper bound determined by hole burning, 0.001 cm^{-1}. With a ZPL dipole moment μ of 1.96(8) D, a Se$^+$ spin in the mode maximum of a cavity with an unloaded Q factor of 1.5×10^4 and a modal volume $V = (\lambda/n)^3$ would display a cooperativity, C, of 1.

D. Raman spectroscopy

The $1s$:$A \Leftrightarrow 1s$:T_2:Γ_7 transition amounts to at least a seven phonon transition, and yet results from Sec. II C 2 show that relaxation from $1s$:T_2:Γ_7 is predominantly nonradiative. Although Altarelli [38] predicted the Se$^+$ $1s$:E state to lie above the $1s$:T_2 state, the Se$^+$ $1s$:E state has not yet been experimentally observed. It is conceivable, but highly unusual, that $1s$:E lies below $1s$:T_2. If $1s$:E were to lie below $1s$:T_2:Γ_7 it could provide a nonradiative decay
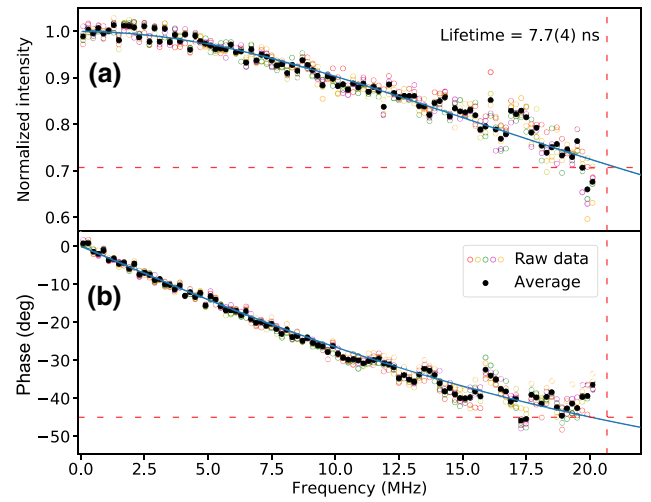

FIG. 5. Excited-state-lifetime measurement of the $1s$:T_2:Γ_7 state of Se$^+$ detected through modulation-frequency-dependent luminescence. Five separate datasets are plotted as open circles and their average is indicated by closed black circles. (a) Amplitude response of the photoluminescence as a function of excitation modulation frequency. The averaged amplitude data are fit with Eq. (4) (blue curve) and the data are normalized to the fit amplitude. (b) Phase response of the photoluminescence as a function of excitation modulation frequency. The phase lag between the AOM drive signal and the luminescence signal is fit with Eq. (5) (blue curve). Dashed red lines intersect the data at the critical modulation frequencies, at which the normalized fit amplitude has dropped to $1/\sqrt{2}$ and phase has lagged by $45°$, revealing a T_1 time for the $1s$:T_2:Γ_7 excited state of 7.7(4) ns.

pathway that could account for the low radiative efficiency of the $1s$:T_2:$\Gamma_7 \Leftrightarrow 1s$:$A$ transition.

The $1s$:$A \Leftrightarrow 1s$:E transition is both EMT forbidden and symmetry forbidden, in contrast with the $1s$:$A \Leftrightarrow 1s$:T_2:Γ_7 transition, which is symmetry allowed, and so indirect methods are needed to deduce the binding energy of the $1s$:E state of both Se^0 and Se$^+$. In the neutral charge state, Se^0, the location of the $1s$:E state has been shown to lie above $1s$:T_2, which for the neutral state Se^0 splits into levels $1s$:$^1T_2$ and $1s$:$^3T_2$ (see Ref. [39]). The position of $1s$:E was extrapolated from strain-induced hybridization of the $1s$:E and $1s$:$^1T_2$ levels [39], with a projected unstrained binding energy of 31.4 meV, corresponding to a $1s$:$A \Leftrightarrow 1s$:E transition of 2220 cm^{-1}. Here we show the results of Raman spectroscopy in an effort to observe forbidden transitions in both Se$^+$ and Se^0, specifically the $1s$:$A \Leftrightarrow 1s$:E transition, which has been observed for shallow donors [40].

Raman spectra of the ^{28}Si:^{78}Se:IB sample [36] are measured with a Bruker IFS 125HR FTIR spectrometer with gold mirrors, a CaF$_2$ beam splitter, and either a liquid-nitrogen-cooled Ge diode detector (for the Se^0 Raman experiments) or a liquid-nitrogen-cooled InSb detector (for Se$^+$ Raman experiments). The InSb detector included a

band-pass filter mounted in the detector's cryogenic assembly to reduce incident room temperature blackbody radiation and increase sensitivity (although the cold-filtered InSb was still much less sensitive than the Ge diode detector). Tunable narrowband 1080-nm ($\sim$9260-cm^{-1}) and 1064-nm ($\sim$9400-cm^{-1}) excitation sources, amplified by an IPG Photonics amplifier (YAR-10K-1064-LPSF), are used to generate the luminescence. In the detection arm, 1150- and 1200-nm long-pass filters were used for laser rejection, with an additional 1100-nm long-pass filter used in the Se^0 Raman experiments.

In Fig. 6(a) we see the results of Raman spectroscopy centered near 7040 cm^{-1}(9260 $-$ 2220 cm^{-1}), where we expect to observe Raman features corresponding to the $1s{:}A \Leftrightarrow 1s{:}E$ transition of Se^0 when laser light near 1080 nm is used. We observe a feature which shifts linearly with laser frequency closely matching the projected value for the $1s{:}A \Leftrightarrow 1s{:}E$ transition. Although unexpected from shallow-donor Raman measurements, we also observe a Raman-active feature that matches the measured value of the $1s{:}A \Leftrightarrow 1s{:}^1T_2$ transition.

We measure an average shift from the laser position of 2223.1(5) cm^{-1} corresponding to $1s{:}A \Leftrightarrow 1s{:}E$, which agrees with the projected strain-free transition frequency of 2220 cm^{-1} from Ref. [39]. We measure an average shift from the laser position of 2195.5(5) cm^{-1}, which agrees with the $1s{:}A \Leftrightarrow 1s{:}^1T_2$ transition energy of 2195.4(5) cm^{-1} directly observed in absorption [see the inset in Fig. 6(a)].

In Fig. 6(b) we show the spectral region where one would expect to observe Raman transitions associated with the $1s{:}A \Leftrightarrow 1s{:}E$ transitions of Se$^+$. Energies labeled $1s{:}E$, denoted by dashed vertical lines in Fig. 6(b), are based on the calculations of Altarelli [38], who predicted the $1s{:}E$ level of Se$^+$ to have a binding energy of approximately 130 meV, corresponding to a $1s{:}A \Leftrightarrow 1s{:}E$ transition near 3740 cm^{-1}. We note no observable feature shifts over the broad range where we would expect to detect Raman Se$^+$ transitions. It is possible that $1s{:}E$ is simply very broad, making it extremely difficult to observe. The $1s{:}A \Leftrightarrow 1s{:}T_2{:}\Gamma_7$ transition is not observed, which agrees with similar shallow-donor Raman experiments. The precise
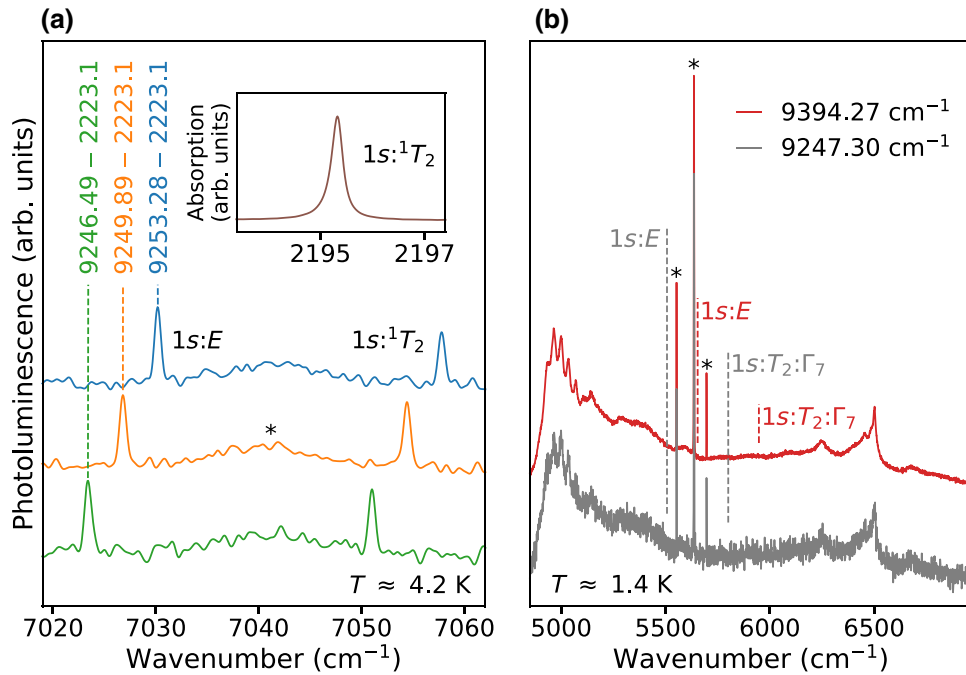

FIG. 6. (a) Raman spectra of the Se^0 region showing features whose shifts in energy match the shifts in tunable laser energy (applied laser energy from bottom to top, 9246.49, 9249.89, and 9253.28 cm^{-1}). The left (right) peaks correspond to Raman scattering from the $1s{:}A \Leftrightarrow 1s{:}E$ ($1s{:}A \Leftrightarrow 1s{:}^1T_2$) transition with an average measured offset of 2223.1 cm^{-1} (2195.5 cm^{-1}) from the applied laser energy. A broad photoluminescence feature of unknown origin is labeled by an asterisk. The spectra are collected with a resolution of 0.5 cm^{-1} with use of a liquid-nitrogen-cooled Ge diode detector. The inset shows the offset due to $1s{:}A \Leftrightarrow 1s{:}^1T_2$ matches the observed energy of the $1s{:}A \Leftrightarrow 1s{:}^1T_2$ transition seen in absorption. (b) Raman spectra of the Se$^+$ donor region revealing no signs of $1s{:}E$ or any other Raman-shifted transitions. Photoluminescence lines corresponding to bound exciton features of unknown origin are marked with an asterisk. Expected Raman-feature positions are indicated with dashed lines under the assumption of the theoretically predicted binding energy of $1s{:}E$ [38] and the known transition energy of $1{:}A \Leftrightarrow 1s{:}T_2{:}\Gamma_7$. The spectra are collected with a resolution of 1.0 cm^{-1} with use of a liquid-nitrogen-cooled InSb detector with a cryogenically mounted band-pass filter.

binding energy of the $1s$:E level of Se$^+$ remains the subject of future investigations.

III. CONCLUSION

We demonstrate that a variety of performance metrics of the ^{77}Se$^+$ spin-photon interface, built upon its $1s$:$A \Leftrightarrow 1s$:T_2:Γ_7 transition, are more favorable than previously thought. A number of key properties of this interface are examined and shown to have encouraging features, including long spin T_1 lifetimes exceeding 4.6(1.5) h at low temperatures and near Earth's magnetic field, a larger transition dipole moment of 1.96(8) D, a $1s$:T_2:Γ_7 excited-state lifetime of 7.7(4) ns, a total radiative efficiency of 0.80(9)%, and a zero-phonon-line fraction of 16(1)%. The Supplemental Material [36] and references therein [41–50] present additional details relevant to these findings.

While the low radiative efficiency prohibits a spin-dependent luminescence read-out scheme, the coupling of the strong dipole moment to an optical cavity can be used to generate a spin-dependent nonlinearity in the strong-coupling regime suitable for entanglement generation and read-out. The spin-dependent cavity cooperativity threshold of 1 may be crossed with routinely achievable photonic cavities having mode volumes of approximately $(\lambda/n)^3$ and Q factors of 1.5×10^4. A broad variety of silicon quantum technologies may be built on the basis of this key and highly-sought-after spin-dependent nonlinearity.

ACKNOWLEDGMENTS

FUNDING

[1] Zhen-Sheng Yuan, Yu-Ao Chen, Bo Zhao, Shuai Chen, Jörg Schmiedmayer, and Jian-Wei Pan, Experimental demonstration of a BDCZ quantum repeater node, Nature **454**, 98 (2008).

[2] S. T. Yílmaz, P. Fallahi, and A. Imamoğlu, Quantum-Dot-Spin Single-Photon Interface, Phys. Rev. Lett. **105**, 033601 (2010).

[3] H. Bernien, B. Hensen, W. Pfaff, G. Koolstra, M. S. Blok, L. Robledo, T. H. Taminiau, M. Markham, D. J. Twitchen, L. Childress, and R. Hanson, Heralded entanglement between solid-state qubits separated by three metres, Nature **497**, 86 (2013).

[4] Kristiaan De Greve, Leo Yu, Peter L. McMahon, Jason S. Pelc, Chandra M. Natarajan, Na Young Kim, Eisuke Abe, Sebastian Maier, Christian Schneider, Martin Kamp, Sven Höfling, Robert H. Hadfield, Alfred Forchel, M. M. Fejer, and Yoshihisa Yamamoto, Quantum-dot spin-photon entanglement via frequency downconversion to telecom wavelength, Nature **491**, 421 (2012).

[5] Lucio Robledo, Lilian Childress, Hannes Bernien, Bas Hensen, Paul F. A. Alkemade, and Ronald Hanson, High-fidelity projective read-out of a solid-state spin quantum register, Nature **477**, 574 (2011).

[6] Brendon C. Rose, Ding Huang, Zi-Huai Zhang, Paul Stevenson, Alexei M. Tyryshkin, Sorawis Sangtawesin, Srikanth Srinivasan, Lorne Loudin, Matthew L. Markham, Andrew M. Edmonds, Daniel J. Twitchen, Stephen A. Lyon, and Nathalie P. deLeon, Observation of an environmentally insensitive solid-state spin defect in diamond, Science **361**, 60 (2018).

[7] Tian Zhong, Jonathan M. Kindem, Evan Miyazono, and Andrei Faraon, Nanophotonic coherent light-matter interfaces based on rare-earth-doped crystals, Nat. Commun. **6**, 8206 (2015).

[8] Manjin Zhong, Morgan P. Hedges, Rose L. Ahlefeldt, John G. Bartholomew, Sarah E. Beavan, Sven M. Wittig, Jevon J. Longdell, and Matthew J. Sellars, Optically addressable nuclear spins in a solid with a six-hour coherence time, Nature **517**, 177 (2015).

[9] David J. Christle, Paul V. Klimov, Charles F. de lasCasas, Valdas Jokubavicius, Jawad Ul Hassan, Mikael Syväjärvi, William F. Koehl, Takeshi Ohshima, Nguyen T. Son, Erik Janzén, Ádám Gali, and David D. Awschalom, Isolated Spin Qubits in SiC with a High-Fidelity Infrared Spin-To-Photon Interface, Phys. Rev. X **7**, 021046 (2017).

[10] Matthias Widmann, Sang-Yun Lee, Torsten Rendler, Nguyen Tien Son, Helmut Fedder, Seoyoung Paik, Li-Ping Yang, Nan Zhao, Sen Yang, Ian Booker, Andrej Denisenko, Mohammad Jamali, S. Ali Momenzadeh, Ilja Gerhardt, Takeshi Ohshima, Adam Gali, Erik Janzén, and Jörg Wrachtrup, Coherent control of single spins in silicon carbide at room temperature, Nat. Mater. **14**, 164 (2014).

[11] S. Strauf, P. Michler, M. Klude, D. Hommel, G. Bacher, and A. Forchel, Quantum Optical Studies on Individual Acceptor Bound Excitons in a Semiconductor, Phys. Rev. Lett. **89**, 177403 (2002).

[12] A. Muller, P. Bianucci, C. Piermarocchi, M. Fornari, I. C. Robin, R. André, and C. K. Shih, Time-resolved photoluminescence spectroscopy of individual Te impurity centers in ZnSe, Phys. Rev. B **73**, 081306 (2006).

[13] Kaoru Sanaka, Alexander Pawlis, Thaddeus D. Ladd, Darin J. Sleiter, Klaus Lischka, and Yoshihisa Yamamoto, Entangling single photons from independently tuned semiconductor nanoemitters, Nano Lett. **12**, 4611 (2012).

[14] X. Linpeng, M. L. K. Viitaniemi, A. Vishnuradhan, Y. Kozuka, C. Johnson, M. Kawasaki, and K.-M. C. Fu, Coherence properties of shallow donor qubits in ZnO, arXiv:1802.03483 [quant-ph] (2018).

[15] Kamyar Saeedi, Stephanie Simmons, Jeff Z. Salvail, Phillip Dluhy, Helge Riemann, Nikolai V. Abrosimov, Peter Becker, Hans-Joachim Pohl, John J. L. Morton, and Mike L. W. Thewalt, Room-temperature quantum bit storage exceeding 39 minutes using ionized donors in silicon-2, Science **342**, 830 (2013).

[16] Gary Wolfowicz, Stephanie Simmons, Alexei M. Tyryshkin, Richard E. George, Helge Riemann, Nikolai V. Abrosimov, Peter Becker, Hans-Joachim Pohl, Stephen A. Lyon, Mike L. W. Thewalt, and John J. L. Morton, Decoherence mechanisms of ^{209}Bi donor electron spins in isotopically pure ^{28}Si, Phys. Rev. B **86**, 245301 (2012).

[17] J. T. Muhonen, A. Laucht, S. Simmons, J. P. Dehollain, R. Kalra, F. E. Hudson, S. Freer, K. M. Itoh, D. N. Jamieson, J. C. McCallum, A. S. Dzurak, and A. Morello, Quantifying the quantum gate fidelity of single-atom spin qubits in silicon by randomized benchmarking, J. Phys.: Condens. Matter **27**, 154205 (2015).

[18] Juan P. Dehollain, Stephanie Simmons, Juha T. Muhonen, Rachpon Kalra, Arne Laucht, Fay Hudson, Kohei M. Itoh, David N. Jamieson, Jeffrey C. McCallum, Andrew S. Dzurak, and Andrea Morello, Bell's inequality violation with spins in silicon, Nat. Nanotechnol. **11**, 242 (2015).

[19] Mohsen K. Akhlaghi, Ellen Schelew, and Jeff F. Young, Waveguide integrated superconducting single-photon detectors implemented as near-perfect absorbers of coherent radiation, Nat. Commun. **6**, 8233 (2015).

[20] A. Mekis, S. Gloeckner, G. Masini, A. Narasimha, T. Pinguet, S. Sahni, and P. De Dobbelaere, A grating-coupler-enabled CMOS photonics platform, IEEE J. Sel. Top. Quantum Electron. **17**, 597 (2011).

[21] M. Hochberg, N. C. Harris, R. Ding, Y. Zhang, A. Novack, Z. Xuan, and T. Baehr-Jones, Silicon photonics: The next fabless semiconductor industry, IEEE Solid State Circuits Mag. **5**, 48 (2013).

[22] M. L. W. Thewalt, A. Yang, M. Steger, D. Karaiskaj, M. Cardona, H. Riemann, N. V. Abrosimov, A. V. Gusev, A. D. Bulanov, I. D. Kovalev, A. K. Kaliteevskii, O. N. Godisov, P. Becker, H. J. Pohl, E. E. Haller, J. W. Ager, and K. M. Itoh, Direct observation of the donor nuclear spin in a near-gap bound exciton transition: ^{31}P in highly enriched ^{28}Si, J. Appl. Phys. **101**, 081724 (2007).

[23] Chunming Yin, Milos Rancic, Gabriele G. de Boo, Nikolas Stavrias, Jeffrey C. McCallum, Matthew J. Sellars, and Sven Rogge, Optical addressing of an individual erbium ion in silicon, Nature **497**, 91 (2013).

[24] Je-Hyung Kim, Shahriar Aghaeimeibodi, Christopher J. K. Richardson, Richard P. Leavitt, Dirk Englund, and Edo Waks, Hybrid integration of solid-state quantum emitters on a silicon photonic chip, Nano Lett. **17**, 7394 (2017)., pMID: 29131963.

[25] J. C. Swartz, D. H. Lemmon, and R. N. Thomas, Optical excitation spectra of selenium-doped silicon, Solid State Commun. **36**, 331 (1980).

[26] H. G. Grimmeiss, E. Janzén, and B. Skarstam, Electronic properties of selenium-doped silicon, J. Appl. Phys. **51**, 3740 (1980).

[27] H. G. Grimmeiss, E. Janzén, and K. Larsson, Multivalley spin splitting of 1s states for sulfur, selenium, and tellurium donors in silicon, Phys. Rev. B **25**, 2627 (1982).

[28] E. Janzén, R. Stedman, G. Grossmann, and H. G. Grimmeiss, High-resolution studies of sulfur- and selenium-related donor centers in silicon, Phys. Rev. B **29**, 1907 (1984).

[29] M. Steger, A. Yang, M. L. W. Thewalt, M. Cardona, H. Riemann, N. V. Abrosimov, M. F. Churbanov, A. V. Gusev, A. D. Bulanov, I. D. Kovalev, A. K. Kaliteevskii, O. N. Godisov, P. Becker, H.-J. Pohl, E. E. Haller, and J. W. Ager, High-resolution absorption spectroscopy of the deep impurities S and Se in ^{28}Si revealing the ^{77}Se hyperfine splitting, Phys. Rev. B **80**, 115204 (2009).

[30] Roberto Lo Nardo, Gary Wolfowicz, Stephanie Simmons, Alexei M. Tyryshkin, Helge Riemann, Nikolai V. Abrosimov, Peter Becker, Hans-Joachim Pohl, Michael Steger, Stephen A. Lyon, Mike L. W. Thewalt, and John J. L. Morton, Spin relaxation and donor-acceptor recombination of Se$^+$ in 28-silicon, Phys. Rev. B **92**, 165201 (2015).

[31] Kevin J. Morse, Rohan J. S. Abraham, Adam DeAbreu, Camille Bowness, Timothy S. Richards, Helge Riemann, Nikolay V. Abrosimov, Peter Becker, Hans-Joachim Pohl, Michael L. W. Thewalt, and Stephanie Simmons, A photonic platform for donor spin qubits in silicon, Sci. Adv. **3**, e1700930 (2017).

[32] Gary Wolfowicz, Alexei M. Tyryshkin, Richard E. George, Helge Riemann, Nikolai V. Abrosimov, Peter Becker, Hans-Joachim Pohl, Mike L. W. Thewalt, Stephen A. Lyon, and John J. L. Morton, Atomic clock transitions in silicon-based spin qubits, Nat. Nanotechnol. **8**, 881 (2013).

[33] G. Feher and E. A. Gere, Electron spin resonance experiments on donors in silicon. II. Electron spin relaxation effects, Phys. Rev. **114**, 1245 (1959).

[34] Theodore G. Castner, Raman spin-lattice relaxation of shallow donors in silicon, Phys. Rev. **130**, 58 (1963).

[35] Theodore G. Castner, Orbach spin-lattice relaxation of shallow donors in silicon, Phys. Rev. **155**, 816 (1967).

[36] See Supplemental Material at http://link.aps.org/supplemental/10.1103/PhysRevApplied.11.044036 for additional information concerning sample creation, determination of impurity concentration, transition-dipole-moment and cooperativity calculations, and impurity conversion factors.

[37] W. Mallawaarachchi, A. N. Davies, R. A. Beaman, A. J. Langleyt, and W. Jeremy Jones, Concentration-modulated absorption spectroscopy part 4. The use of continuous-wave lasers, J. Chem. Soc. Faraday Trans. **2**, 707 (1987).

[38] M. Altarelli, Excited states of double donors in silicon, Physica B+C **117**, 122 (1983).

[39] G. Grossmann, K. Bergman, and M. Kleverman, Spectroscopic studies of double donors in silicon, Physica B+C **146**, 30 (1987).

[40] G. B. Wright and A. Mooradian, Raman Scattering from Donor and Acceptor Impurities in Silicon, Phys. Rev. Lett. **18**, 608 (1967).

[41] G. G. Devyatykh, A. D. Bulanov, A. V. Gusev, I. D. Kovalev, V. A. Krylov, A. M. Potapov, P. G. Sennikov, S. A. Adamchik, V. A. Gavva, A. P. Kotkov, M. F. Churbanov, E. M. Dianov, A. K. Kaliteevskii, O. N. Godisov, H. J. Pohl, P. Becker, H. Riemann, and N. V. Abrosimov, High-purity

single-crystal monoisotopic silicon-28 for precise deter-mination of Avogadro's number, Dokl. Chem. **421**, 157 (2008).

[42] Cheol-Seong Kim, Eiji Ohta, and Makoto Sakata, Electrical properties of selenium-diffused silicon, Jpn. J. Appl. Phys. **18**, 909 (1979).

[43] E. Schibli and A. G. Milnes, Deep impurities in silicon, Mater. Sci. Eng. **2**, 173 (1967).

[44] Cheol-Seong Kim and Makoto Sakata, Diffusion coefficient of selenium in silicon by sheet Hall coefficient measure-ment, Jpn. J. Appl. Phys. **18**, 247 (1979).

[45] Peter Pichler, *Intrinsic Point Defects, Impurities, and Their Diffusion in Silicon* (Springer-Verlag, Vienna, 2004), 1st ed...

[46] S. Zakel, S. Wundrack, H. Niemann, O. Rienitz, and D. Schiel, Infrared spectrometric measurement of impu-rities in highly enriched 'Si28', Metrologia **48**, S14 (2011).

[47] Zhiyi Yu, Spin-orbit splitting of the valence bands in silicon determined by means of high-resolution photoconductive spectroscopy, Phys. Rev. B **39**, 6287 (1989).

[48] P. G. Sennikov, T. V. Kotereva, A. G. Kurganov, B. A. Andreev, H. Niemann, D. Schiel, V. V. Emtsev, and H. J. Pohl, Spectroscopic parameters of the absorption bands related to the local vibrational modes of carbon and oxy-gen impurities in silicon enriched with ^{28}Si, ^{29}Si, and ^{30}Si isotopes, Semiconductors **39**, 300 (2005).

[49] Robert C. Hilborn, Einstein coefficients, cross sections, *f* values, dipole moments, and all that, Am. J. Phys. **50**, 982 (1982).

[50] Bradley J. Frey, Douglas B. Leviton, and Timothy J. Madison, Temperature-dependent refractive index of sili-con and germanium, in *Optomechanical Technologies for Astronomy* (SPIE Astronomical Telescopes and Instrumen-tation, Orlando, Florida, United States, 2006), Vol. 6273, p. 62732J.